

Journal Pre-proof

A mean-field phase separation model enabling the coupling of non-isothermal flow phenomena with fibre formation in high-moisture extrusion of meat analogues

Erik Kaunisto, Camilla Öhgren, Niklas Lorén, Mats Stading



PII: S0260-8774(26)00010-5

DOI: <https://doi.org/10.1016/j.jfoodeng.2026.112972>

Reference: JFOE 112972

To appear in: *Journal of Food Engineering*

Received Date: 20 August 2025

Revised Date: 5 January 2026

Accepted Date: 7 January 2026

Please cite this article as: Kaunisto, E., Öhgren, C., Lorén, N., Stading, M., A mean-field phase separation model enabling the coupling of non-isothermal flow phenomena with fibre formation in high-moisture extrusion of meat analogues, *Journal of Food Engineering*, <https://doi.org/10.1016/j.jfoodeng.2026.112972>.

This is a PDF of an article that has undergone enhancements after acceptance, such as the addition of a cover page and metadata, and formatting for readability. This version will undergo additional copyediting, typesetting and review before it is published in its final form. As such, this version is no longer the Accepted Manuscript, but it is not yet the definitive Version of Record; we are providing this early version to give early visibility of the article. Please note that Elsevier's sharing policy for the Published Journal Article applies to this version, see: <https://www.elsevier.com/about/policies-and-standards/sharing#4-published-journal-article>. Please also note that, during the production process, errors may be discovered which could affect the content, and all legal disclaimers that apply to the journal pertain.

© 2026 Published by Elsevier Ltd.

1 **Title:** A mean-field phase separation model enabling the coupling of non-isothermal flow phenomena
2 with fibre formation in high-moisture extrusion of meat analogues

3

4 **Author names:** Erik Kaunisto¹, Camilla Öhgren¹, Niklas Lorén¹ and Mats Stading^{1,2}

5 ¹RISE – Research Institutes of Sweden AB, Department of Food Science and Innovation, Gothenburg,
6 Sweden

7 ²Chalmers University of Technology, Department of Industrial and Materials Science, Gothenburg,
8 Sweden

9

10 **Corresponding author:** Mats Stading

11

12 **Highlights:**

13 • The model enables coupling relevant non-isothermal flow phenomena with fibre formation in
14 the cooling die during high moisture extrusion.

15 • The impact of cooling temperature on plug flow transition is explained through a mean-field
16 phase separation/syneresis dependent wall-slip condition.

17 • A simple shear history-dependent fibre alignment measure is proposed that enables a
18 composite measure of fibre formation.

19 • Qualitative agreement between microscopy data and the location of predicted oriented and
20 randomly oriented fibre domains in the extrudate is obtained.

21 • The model offers a practical coarse-grained alternative to solving the Cahn-Hilliard equation for
22 prediction of fibre formation.

23

24 **Abstract:**

25 In this study, a coupled model integrating flow, temperature, phase separation, fibre alignment, and
26 wall-slip has been developed to elucidate the complex behaviour observed during high moisture
27 extrusion (HME) fibre formation. By departing from previous high-resolution approaches, the model
28 uses a mean-field simplification to conveniently address wall-slip, thus avoiding the numerical
29 intractability associated with resolving microscopic phases through solving the full Cahn-Hilliard
30 equations. The critical simulation parameters are justified through prior studies and microscopy data
31 and may to a certain extent be quantifiable from dead-stop experiments. The model can capture key
32 qualitative features of HME, including the spatial distribution of fibres in the cooling die and their
33 orientation, as observed in microscopy. Moreover, the model explains a potential delicate interplay
34 between die cooling, phase separation/syneresis and protein melt flow characteristics. The study
35 identifies extensional and pre-cooling die orientation of fibres as promising avenues for future model
36 refinement.

37

38 **Keywords:** Meat analogues, High moisture extrusion, Phase separation, Wall-slip, Simulation, Finite
39 element model, Microscopy

40

41 1. Introduction

42 Global meat consumption has doubled from 1961 to 2009 and is still on the rise (Steinfeld, 2006).
43 The food sector is responsible for 25% of all greenhouse gas emissions, with meat production alone
44 accounting for a significant 14.5% (Gerber et al., 2013). This surge in meat consumption is concerning
45 from a nutritional standpoint as well, as excessive intake of especially red meat has been associated
46 with health issues like coronary heart disease and certain types of cancer (Di et al., 2023; Glenn et al.,

47 2024; Tammi et al., 2024). Plant-based alternatives to meat, meat-analogues, are for these and other
48 reasons gaining popularity.

49 Fibrous meat-analogues are currently produced commercially from soy and pea protein, as well as
50 from wheat gluten, using an extruder to create a protein melt under high moisture, temperature,
51 and pressure, followed by active cooling upon exit. Similar fibre formation techniques are used in
52 plastics production to enhance material strength (Ardakani et al., 2013). A common factor in fibre
53 formation for both meat analogues and plastics is that the production process is known, but the
54 mechanisms behind fibre formation are not fully understood. Existing hypotheses on the
55 mechanisms provide insights but are insufficient for a complete explanation and cannot fully predict
56 the fibre formation capability of protein melts. This limitation hinders the use of more sustainable
57 protein sources in meat analogue production and limits the speed of processing. Hypotheses and
58 models range from "chemical," highlighting the interactions between protein chains or polymer
59 crystallites, to "physical," focusing on fluid dynamics, heat transfer, phase separation, melt fracture
60 and deserve a more detailed presentation, as further elaborated upon below.

61 Structural effects of covalent and non-covalent bonds has been studied, but does not provide a
62 concrete kinetic fibre formation mechanism (Chen et al., 2011). In another model, extensional,
63 kinetic energy and Poisson's ratio-based mechanisms have been investigated for
64 polytetrafluoroethylene (PTFE) and refer fibre formation to a consequence of forced attraction
65 between polymer particles by extensional flow, thus neglecting the possible significance of shear
66 contributions (Ardakani et al., 2013; Patil et al., 2006; Vavlekas et al., 2017). The model is highly
67 relevant for the structure formation in PTFE, but as it describes fibre formation as reversible the
68 relevance is limited for extrusion of high moisture meat analogues (HMMA).

69 Several groups have proposed models based on phase separation coupled with heat transfer and
70 mechanical deformation (Kaunisto et al., 2024; Sandoval Murillo et al., 2019; van der Sman and van
71 der Goot, 2023; Wittek et al., 2021). The cooling die cools the melt from the outside causing high

72 melt viscosity along the walls and effectively a funnel-shaped flow profile with high flow of hot melt
73 in the centre of the die and slow flow of cold melt along the walls (Högg et al., 2017; Kaunisto et al.,
74 2024; Osen and Schweiggert-Weisz, 2016; Sandoval Murillo et al., 2019). This causes extensional flow
75 in the centre and high shear in the transition zone between cold and hot melt flow. Structure
76 formation is assumed to arise from phase separation into a protein-rich and a protein-poor phase
77 under a critical temperature, and can be described by the Cahn-Hilliard model (Cahn and Hilliard,
78 1958). The phase separation has been simulated under the assumption of spinodal decomposition
79 (Kaunisto et al., 2024; Sandoval Murillo et al., 2019), and has alternatively been suggested to possibly
80 depend on cross-linking (van der Sman and van der Goot, 2023). The Cahn-Hilliard model only
81 postulates phase separation under a critical temperature, but an underlying multi-phase system has
82 also been suggested to occur already in the hot screw section of the extruder, based on dead-stop
83 experiments (Wittekk et al., 2021). The fibrous structure induced by the phase separation was
84 simulated and fibres were found to align in the high-shear flow regions of the cooling die (Kaunisto et
85 al., 2024; Sandoval Murillo et al., 2019). The shear structuring has been thoroughly studied by the
86 Van der Goot group, but in a shear-cell rather than in an extruder cooling die (Cornet et al., 2022;
87 Dekkers et al., 2018; Grabowska et al., 2014).
88 The fibrous structure in HMMA has also been suggested to arise from viscoelastic mass fracture
89 arising from flow instabilities such as melt-fracture trapped by distinct solidification (Guan et al.,
90 2024; Sägesser et al., 2025). A sudden drop in shear viscosity was observed when shearing soy-
91 protein and pea protein melts in a high pressure cell (Sägesser et al., 2025).
92 High moisture extrusion (HME) of HMMA has two main experimental challenges in validating any of
93 the suggestions and models: harsh conditions in the extruder and the instable nature of the
94 extrudates. Extrusion is typically performed at temperatures up to 150°C and high pressure like 10
95 bars, which is difficult to reproduce in any experimental technique. Furthermore, any experimental
96 method that should mimic extruder conditions must involve significant deformation, as that drives
97 structure formation. The extrudates in themselves also pose a challenge. Pulled pork can be used as

98 a metaphor in explaining the dilemma. It appears solid and structureless until deformed, and when
99 pulled apart the fibres appear. The extrudates appear solid and fibres appear only when the
100 extrudates are deformed, frozen-thawed or swelled (Lorén et al., 2025; Nieuwland et al., 2023).

101 Meso-scale areas formed by phase separation or other mechanisms have only been visualised after
102 freezing or sample preparation (Lorén et al., 2025).

103 Experiments for validating models should preferably be performed directly in the extruder and the
104 cooling die and there are a few reported results. A small extruder and cooling die was placed in a
105 neutron beamline to elucidate nano-scale structure development during extrusion (Guan et al.,
106 2024). Globular proteins (~9nm) and nanoaggregates (~40nm) were found throughout the cooling
107 die and no further structuring at the nanoscale was observed. Flow profiles have been obtained

108 directly in the cooling die using pulsed ultrasound velocity profiling (Kaunisto et al., 2025). Velocity
109 profiles were accurately reproduced but the resolution close to the die wall was not sufficient to
110 validate the bell-shaped velocity profiles predicted by simulation (Kaunisto et al., 2024). A popular

111 experimental technique is “dead-stop” experiments, with or without added dyeing of the material,
112 where the extruder is suddenly stopped, opened and samples collected along the extruder screws
113 and in the cooling die (Chen et al., 2011; Högg et al., 2025; Wittek et al., 2021; Zhang et al., 2022). It

114 gives information along the whole extrusion process such as arrested flow profiles and chemical
115 composition, but as the method suddenly release the high pressure and drops the temperature it
116 may change structures in the melt. The process also takes several minutes so the non-equilibrium
117 state in the extruder will have time to relax.

118 In the present study we have added the effect of wall-slip on fibre formation to previously described
119 mechanisms by using a practical and computationally faster mean-field simplification to avoid the
120 numerical and theoretical difficulties associated with solving the Cahn Hilliard equations under wall-
121 slip. The present study aims to couple wall-slip to phase separation mechanism, to explain an
122 interplay between die cooling, phase separation/syneresis and protein melt flow characteristics.

123

124 2. Materials and methods

125 2.1. Experimental input data

126 The present study uses the same experimental input data and assumptions for pea protein from
 127 rheological measurements and literature, as we have previously presented (Kaunisto et al., 2024).

128 The obtained power-law exponent for the protein melt at 62% moisture content was $n = 0.13$ and
 129 the temperature dependence followed an Arrhenius-type expression, given in equation (1) below for
 130 convenience,

131

$$132 K(T) = z_1 * e^{\frac{z_2}{z_3 + T}} \quad (1)$$

133

134 where $z_1 = 100.2$, $z_2 = 637.9$ and $z_3 = 28.4$ with T in degrees Celsius. The physical properties of the
 135 protein melt were $C_p = 3.39 \frac{kJ}{[KgK]}$, $k = 0.43 \frac{W}{[mK]}$ and $\rho = 1000 \left[\frac{kg}{m^3} \right]$, as defined in Section 3.2,
 136 giving a thermal diffusion coefficient $\alpha = \frac{k}{\rho C_p} \approx 0.127 \frac{mm^2}{s}$. The reader is referred to the previous
 137 study for more experimental details (Kaunisto et al., 2024).

138

139 2.2. Microscopy of extrudate samples

140 2.2.1. Light microscopy

141 Microscopy data was obtained for extrudates at similar extrusion operating conditions, as mentioned
 142 in our previous study (Kaunisto et al., 2024) to enable a qualitative comparison with the simulations.
 143 A light microscope (LM, Olympus BX53F2) equipped with a CMOS colour camera (Olympus SC50) and
 144 the software Olympus CellSense Entry was utilized to visualize the extruded samples at different
 145 positions in the samples and from different directions. The samples were analysed using 4x, 10x, 20x,

146 40x and 100x objectives. The samples were prepared as follows: The extrudates were cut into pieces
147 of approximately 1 x 2 x 4 mm in two different directions related to the extrusion direction. The
148 rectangular blocks were airfixed by lying on a grid above formalin and glutaraldehyde in CaO₃ for 3
149 days in a closed chamber. The third day they were placed above 2% OsO₄ for 3h. In a graded series of
150 ethanol solutions (50, 70, 90 and 100% by volume) the samples were dehydrated at room
151 temperature and subsequently embedded in epoxy resin (Technovit 7100). Sections of 1.0 µm were
152 cut with an RMC Power Tome XL using glass knives; the samples were subsequently placed on glass
153 slides. The sections were stained with Lugol's iodine solution to visualise the starch phase and the
154 dye Light Green in acetic acid was used to visualise the protein phase.

155

156 2.2.2. Confocal laser scanning microscopy
157 The extrudates were stained with 0.01% Texas Red solution and Direct Yellow 96. Micrographs were
158 acquired using confocal laser microscopy (CLSM; Leica TCS SP5, Heidelberg, Germany). A 488 nm
159 argon laser and a 594 nm HeNe laser and an HCX PL APO CS 10.0x 0.40 DRY UV objective, was used.
160 Emissions were collected at 500–540 and 610–650 nm using an image format 1024 x 1024 pixels with
161 an eight lines average.

162

163 3. Calculation and theory

164 3.1. Model and geometry assumptions

165 The present work uses similar model assumptions as we have previously presented (Kaunisto et al.,
166 2024), where the fibre formation process can be effectively regarded as a phase separation process,
167 although possibly connected to the hypothesized syneresis and solidification mechanisms in the
168 cooling die (van der Sman and van der Goot, 2023). Further, the 2D parallel plate assumption is used

169 (Kaunisto et al., 2024), where the half-width and length are set as 2.5 mm and 200 mm, respectively,
 170 in accordance with one modular section of the updated cooling die studied here.

171

172 3.2. Mathematical model

173 3.2.1. Flow and temperature

174 The flow field is modelled as previously (Kaunisto et al., 2024) and stated here again for convenience.
 175 The stationary incompressible Navier-Stokes (NS) equations (2–3) are coupled to a calibrated
 176 temperature-dependent constitutive power-law model (4–5) and the associated stationary
 177 temperature field (6),

178

$$179 \rho \mathbf{u} \cdot \nabla \mathbf{u} = -\nabla p + \nabla \cdot [\mu_{eff} (\nabla \mathbf{u} + (\nabla \mathbf{u})^T)] \quad (2)$$

$$180 \nabla \cdot \mathbf{u} = 0 \quad (3)$$

$$181 \mu_{eff} = K(T) \dot{\gamma}^{n-1} \quad (4)$$

$$182 \dot{\gamma} = \sqrt{2u_x^2 + (v_x + u_y)^2 + 2v_y^2} \quad (5)$$

$$183 \rho C_p \mathbf{u} \cdot \nabla T = \nabla \cdot (k \nabla T) \quad (6)$$

184

185 where ρ is the mass density, $\mathbf{u} = (u, v)$ is the flow field, p is the pressure, μ_{eff} is the effective
 186 viscosity, K is the consistency index, n the power-law exponent, T the temperature, $\dot{\gamma}$ the strain-rate
 187 scalar, C_p is the specific heat capacity and k the thermal conductivity. It can be noted that the
 188 definition of the strain-rate scalar in equation (5) follows that of Slattery (Slattery, 1999),
 189 corresponding to the strain rate in viscometric flows. Further, in the constitutive model, the
 190 temperature dependency is assumed to be carried solely by the consistency index parameter, similar

191 to other work (Wittekk et al., 2021). The main reason for working with a power-law constitutive model
 192 is, to the best of our knowledge, a lack of evidence in the literature for the significance of
 193 elongational effects in HMMA fibre formation. Another important reason is that such models are
 194 often hard to calibrate from available experimental data and may exhibit limited shear-thinning
 195 behaviour, as compared to the experimentally observed $n = 0.1 - 0.2$.

196

197 3.2.2. Simplified phase separation model

198 As an alternative to using a thermodynamic potential when solving the Cahn-Hilliard equations for a
 199 random instantiation of the phase separated state in the extruder die (Kaunisto et al., 2024), the
 200 same thermodynamic potential was instead used as the basis to develop a simplified phase
 201 separation model to account for fibre formation. The thermodynamic potential is stated in equation
 202 (7) below for convenience.

203

$$204 \quad \Psi = 2T_c R c (1 - c) + T R [(1 - c) \ln(1 - c) + c \ln(c)] \quad (7)$$

205

206 where $c = \frac{\phi+1}{2}$ is the concentration, ϕ is the order parameter, Ψ the symmetric thermodynamic
 207 potential, T_c the critical temperature, T is the temperature and R the gas constant. The local
 208 equilibrium phase separation, $\beta_{eq} = |\phi_0|$, was calculated numerically by setting $\frac{\partial \Psi}{\partial \phi} = 0$, and solving
 209 for the order parameter, $\pm \phi_0$, for specific values of T and T_c . An explicit expression, equation (8),
 210 was then fitted over the relevant potential temperature ranges, see Figure 1,

211

$$212 \quad \beta_{eq}(T_c, T) = \begin{cases} (p_1 T_c^2 + p_2 T_c + p_3) \tanh[(p_4 T_c^2 + p_5 T_c + p_6)(T_c - T)]^{(p_7 T_c + p_8)}, & \text{for } T < T_c \\ 0, & \text{for } T \geq T_c \end{cases} \quad (8)$$

213

214 where $p_1 = -4.33 \times 10^{-5}$, $p_2 = 1.16 \times 10^{-2}$, $p_3 = 1.94 \times 10^{-1}$, $p_4 = 1.50 \times 10^{-6}$, $p_5 =$
 215 -4.00×10^{-4} , $p_6 = 3.40 \times 10^{-2}$, $p_7 = -1.48 \times 10^{-4}$ and $p_8 = 5.07 \times 10^{-1}$ are the fitted
 216 parameters, as determined by non-linear regression. The use of a hyperbolic tangent construction is
 217 a natural choice due to the inherent symmetry, smoothness and sigmoid-like behaviour of the phase
 218 transition, as governed by the thermodynamic potential. Figure 1 shows that equation (8) accurately
 219 captures the equilibrium order parameter to be conveniently used in a simplified phase separation
 220 model for any given and valid T_c . Thus, a stationary mean-field transport equation for the local
 221 amount of phase separation can be formulated according to equation (9)

222

$$223 -\nabla \cdot \left[\frac{0.1D(T_c)K(T_c)}{K(T)} \nabla \beta \right] + \mathbf{u} \cdot \nabla \beta = \frac{D(T_c)}{\varepsilon^2} \frac{K(T_c)}{K(T)} (\beta_{eq}(T_c, T) - \beta) \quad (9)$$

224

225 where β is the local amount of phase separation, defined on the interval $[0,1]$, ε is the characteristic
 226 distance between phase separated domains and $D(T_c) = 0.1\alpha$ is the diffusion coefficient with an
 227 associated scaling with the consistency index, as previously discussed by Kaunisto et al. 2024 and
 228 Murillo et al. 2019 (Kaunisto et al., 2024; Sandoval Murillo et al., 2019). Equation (9) accounts for the
 229 local average production and convection of phase separated fluid material with a relatively small
 230 added diffusion term for numerical smoothing. It should be noted here that the characteristic
 231 distance between phase separated domains needs to be small enough for the present coarse-grained
 232 model to be arguably valid and that interfacial surface tension and gradient penalization effects are
 233 not explicitly modelled.

234

235 An inherent challenge with using a scalar field to represent fibre formation is the lack of orientational
 236 information regarding fibre alignment, which is crucial for the texture of HMAs. Recent literature

237 suggests that fibres are likely the result of multiscale texturization mechanisms (van der Sman and
 238 van der Goot, 2023), including non-isothermal shear flow, making it arguably non-trivial to define a
 239 meaningful fibre orientation through a conformation tensor approach, such as the Folgar-Tucker
 240 model (Folgar and Tucker, 1984). However, it seems reasonable that the local accumulated shear in
 241 the cooling die could act as an approximation of the amount of multiscale fibre alignment that can be
 242 expected. Therefore, an additional simple transport equation (10) is proposed,

243

$$244 -\nabla \cdot \left[\frac{0.1D(T_c)K(T_c)}{K(T)} \nabla \theta \right] + \mathbf{u} \cdot \nabla \theta = \frac{\dot{\gamma}(1-\theta)}{\theta_{res}} \quad (10)$$

245

246 where θ is the fibre alignment measure defined on the interval $[0,1]$, and θ_{res} is the fluid resistance
 247 to alignment. Equation (10) assumes that alignment is produced by the local effective shear, i.e. the
 248 shear rate for viscometric flows. With both β and θ defined, it is possible to define the oriented and
 249 randomly oriented fibre composite measures of the fluid as $F_o = \beta\theta$ and $F_{ro} = \beta(1 - \theta)$,
 250 respectively, i.e. combining the effects of shear-induced fibre alignment and preservation of the
 251 structure through phase separation-induced solidification.

252

253 3.2.3. Boundary conditions

254 The non-trivial boundary conditions in the present model are summarised in Figure 2, showing the
 255 solution domain, Ω , and associated boundaries, $d\Omega_i$ for $i = 1, 2, 3, 4, 5$. Dirichlet conditions are used
 256 to specify assumed fully developed flow, \mathbf{u}_{inlet} , the inlet temperature, $T_{inlet} = 140\text{ }^\circ\text{C}$, phase
 257 separation, $\beta_{inlet} = 0$ and alignment, $\theta_{inlet} = 0$, at the inlet boundary $d\Omega_1$. A no-slip condition is
 258 used over the initial part of the cooling die, $d\Omega_2$, followed by a phase separation dependent wall-slip
 259 and a Dirichlet condition for the cooling temperature that are imposed on the remainder of the die
 260 length, $d\Omega_3$. The expression for the slip length, L , is based on a smooth ramping function, where a

261 finite asymptotic slip length, $L_0 = 20\text{ mm}$, and a regularization parameter, $\kappa = 1\text{ mm}$, are assumed
 262 to model the slip behaviour and to avoid numerical problems for low values of β . The physical
 263 justification for the current wall-slip condition is the hypothesized syneresis/solidification mechanism
 264 that expels water at the surface, thus creating a slippery surface. A symmetry condition is further
 265 imposed at the half-channel width, $d\Omega_4$, and at the die exit, $d\Omega_5$, a zero-pressure regular outlet
 266 condition is specified. In all other cases, and if not specified in Figure 2, a natural boundary condition
 267 is used.

268

269 3.2.4. Numerical implementation

270 The model is cast on weak form and implemented in COMSOL Multiphysics 6.3 (COMSOL, 2021),
 271 using a combination of existing fluid and heat flow interfaces and two custom PDE interfaces for a
 272 straightforward implementation of the simplified phase separation and alignment equations. Before
 273 solving, the necessary fitting parameters in equation (8) were generated with a simple MATLAB script
 274 and the smooth ramping function for the slip-condition was defined in COMSOL in terms of its
 275 dimensionless position and transition length arguments, 0.5 and 1, respectively, yielding values over
 276 the interval $[0, 1]$ for a given β . The stationary model was then solved by using the PARDISO
 277 stationary parametric solver, where the wall temperature was ramped down from the inlet
 278 temperature to the specified wall cooling temperature. The initial guess for the solution variables
 279 was a fully developed velocity profile, $\mathbf{u} = \mathbf{u}_{inlet}$, $T = T_{inlet}$, $\beta = \beta_{inlet}$ and $\theta = \theta_{inlet}$. A mesh
 280 density of approximately 140,000 triangular mesh elements over the given solution domain (see
 281 section 3.1 and Figure 2) was used to solve all the equations. The equation system was quite stiff
 282 with a solution time in the order of days on an Intel® Xeon® w5-3435X, 3096 MHz, 16 Core(s), 32
 283 Logical Processor(s) with 256 GB RAM, depending on parameter settings. Mesh convergence was also
 284 checked for the flow variables to ensure a converged solution.

285

286 4. Results

287 4.1. Impact of cooling temperature

288 4.1.1. Additional simulation parameters

289 The model was used to study the impact of cooling temperature on the flow profiles in the extruder
 290 die and specifically at the extruder die outlet. A maximum inlet velocity of 5 mm/s and critical
 291 temperature for phase separation, $T_c = 110 \text{ }^\circ\text{C}$, was specified in accordance with previous studies
 292 (Kaunisto et al., 2024; Sandoval Murillo et al., 2019). In addition, a characteristic distance between
 293 phase separated domains, $\varepsilon = 50 \mu\text{m}$, and a fluid resistance to alignment, $\theta_{res} = 100$. The values of
 294 the latter two parameters are further discussed in relation to Section 4.3 and Section 5.

295

296 4.1.2. Extruder die flow profile

297 The effect of varying cooling temperature on the velocity profile in the extruder die is shown in
 298 Figure 3. Figure 3A shows small initial deviations from the fully developed inlet flow profile already at
 299 a cooling temperature corresponding to the critical temperature of 110 $^\circ\text{C}$, where the flow exhibits a
 300 weak initial core slip caused by the formation of a viscosity-induced funnel, as earlier pointed out
 301 (Kaunisto et al., 2024), where recovery of the inlet flow profile is then achieved towards the end of
 302 the die due to limited cooling. On the other hand, in Figure 3B, the initial core slip is stronger by the
 303 lowered cooling temperature, resulting in both relatively higher thermal penetration and phase
 304 separation that, in turn, causes wall-slip and a transition towards plug flow. In contrast to Figure 3A,
 305 continuity and loss of wall-shear require the peripheral streamlines to bend significantly from the
 306 high-shear initial core-slip region of Figure 3B towards the sides of the die, whereas the central
 307 streamlines remain essentially unaffected. When the fluid is further cooled, the initial core-slip and
 308 central velocity are too strong, implying that thermal penetration, phase separation and wall-slip
 309 cannot manage to recover the plug flow over the remainder of the die, as shown in Figure 3C.

310

311 4.1.3. Die outlet velocity profile

312 The shape of the velocity profile at the outlet was investigated for different cooling temperatures, as
313 illustrated in Figure 4. For higher cooling temperatures, the velocity profile shows a regular shear-
314 thinning velocity profile with higher velocity gradients at the wall due to the low wall-slip. However,
315 close to a cooling temperature of 90 °C, the flow reaches almost plug flow like behaviour and then
316 switches to an s-shape, with stronger core-slip, at even lower cooling temperatures. The results in
317 Figure 3-4 thus provide a potential explanation for the delicate interplay between protein melt
318 rheology, wall-slip, thermal penetration and phase separation to yield optimal conditions for fibre
319 formation during high moisture extrusion.

320

321 4.2. Fibre formation

322 4.2.1. Local amount of phase separation

323 To further explain the onset of wall-slip, the local amount of phase separation in the extruder die was
324 assessed. In Figures 5A-C, phase separation is plotted against three different cooling temperatures,
325 illustrating the varying degree of solidification and thermal penetration. In Figure 5A, the subcooling
326 below the critical temperature is too low, causing limited phase separation towards mainly the edges
327 of the die and a weak wall-slip. In Figure 5B, the flow situation is that of Figure 3B where wall-slip
328 increases, yielding longer residence times towards the end of the die, improved thermal penetration
329 and phase separation. With further subcooling in Figure 5C with the corresponding flow situation in
330 Figure 3C, the thermal penetration is indeed further increased, causing more phase separation at the
331 edges and in the core towards the end of the die, but the resulting core-slip and lack of plug flow
332 would make the associated operating conditions unfeasible in this case.

333

334 4.2.2. Fibre alignment measure

335 To investigate how the fluid is subjected to shear-induced fibre alignment, the associated measure
336 was plotted for the same temperatures as in Figure 5, see Figure 6. Alignment is being produced
337 already at walls in the fully developed inlet region in Figures 6A-C with a broadening of the
338 production region towards the centre of the cooling die. In Figure 6B the alignment seems to be
339 gradually produced in the cooled fluid region closer to the walls, either due to the longer residence
340 times or the higher shear in the transition towards the inner core. When the plug flow is formed due
341 to increasing slip, the alignment is further advected along the streamlines to the walls, for reasons of
342 continuity, thus contributing to a potential gradual concentration of alignment in this region and
343 along the length of the cooling die. In Figure 6C the alignment is even more pronounced towards the
344 centre of the cooling die, although not feasible, as previously mentioned.

345

346 4.2.3. Composite fibre measure

347 The local amount of phase separation and resistance to fluid alignment were used to assess the
348 composite measures of fibre formation, see Figure 7. From Figures 7A-B it is evident that the present
349 model predicts oriented fibres close to the walls and randomly oriented fibres in the core. These
350 results are consistent with our previous simulation results (Kaunisto et al., 2024), although with the
351 added refinement of accounting for the non-trivial effects of wall-slip. Notably though, the oriented
352 fibres are quickly and continuously formed along the cooling die, whereas the die length and
353 transition to plug flow both contribute to the increased thermal penetration and formation of the
354 randomly oriented fibres.

355

356 4.3. Light microscopy and model validation

357 To validate the model, extrudates have been studied visually on the micrometre scale, see Figure 8A,
358 where a planar image of the extrudate with a perspective as in the simulations has been generated

359 by cutting from the side and about 1 cm into the sample. Figures 8B-D show how the structure looks
360 near either the bottom or the top edge of the extrudate, while Figure 8E shows the structure in the
361 middle. As can be seen in Figure 8A, the extrusion direction (from left to right) in the sample is visible
362 and protein fibre strands are delimited by areas that contain either a lower proportion of protein or
363 bran components or starch. At an overall level of structure in the CLSM image in Figure 8B and in the
364 LM image in Figure 8C, with slightly higher magnification, the protein is seen to form fibres with an
365 average width of about 40-80 μm , which corresponds well with a characteristic distance between
366 phase separated domains of 50 μm . The LM image in Figure 8D shows the oriented protein phase
367 close to the top or bottom edges at high magnification, while the LM-image in Figure 8E shows a
368 more randomly distributed protein phase, which is obtained from the middle of the extrudate, at the
369 same magnification. The fact that different degrees of fibre orientation are obtained at different
370 positions is in good agreement with the simulation model.

371

372 5. Discussion

373 The present study aims to couple flow, temperature, phase separation, fibre alignment and wall-slip
374 to explain observed flow and fibre formation characteristics during HME extrusion, where the model
375 simplifications, as compared to previous work, deserve to be discussed. In this regard, it is important
376 to emphasize that solving e.g. the full Cahn-Hilliard equations for a time-dependent random
377 instantiation of the phase separated state is of practical limited value when formulating a simplified
378 wall-slip condition. That is, if the microscopic details of the phases are resolved by an alternative
379 model, and thus allowed to randomly alternate at the wall, both viscosity and the wall condition
380 should vary significantly over very small length scales. The latter would make the model numerically
381 intractable, and the present mean-field approach therefore seems to be a reasonable compromise to
382 account for wall-slip. However, if phase separation is considered fast, one could consider just solving
383 equation (8) algebraically for the equilibrium value to reduce the numerical complexity of the model,

384 and for direct use in the boundary condition for the wall-slip. Such an approach would imply that the
385 temperature would act as the natural proxy variable for phase separation, which would disregard any
386 significant resistances to mass transfer at the boundary.

387 Regarding the temperature boundary condition, it should also be mentioned that a cooling
388 temperature of 100-110 °C naturally requires pressurized water or another medium. This is
389 considered a detail, as the model parameters likely need to be calibrated so that the model predicts
390 the same behaviour over other temperature ranges, as observed in any experiment. From previous
391 studies and measurements, we have tried to justify the chosen simulation parameters, except for the
392 fluid resistance to alignment. In principle, resistance to alignment could potentially be quantifiable to
393 some degree from a dead-stop experiment, since unintentional fast solidification of the structure
394 from flash cooling should preserve alignment, in contrast to the amount of phase separation.

395 Nonetheless, the parameters chosen in this study are deemed sufficient to indicate the potential
396 non-linear phenomena of fibre formation to be expected during HME. Importantly, from the light
397 microscopy images of the extrudate cross-section, it can be concluded that the characteristic
398 distance in the present study seems feasible. Moreover, the present study manages to qualitatively
399 explain the observed distinction of oriented fibre and randomly oriented fibre domains close to the
400 die wall and in the centre, respectively, where the creation and transport of alignment seems to play
401 an important role.

402 As an alternative to the present model, one could assume that fibre formation and wall-slip is only
403 dependent on e.g. temperature, local shear, critical shear stress and a fibre conformation tensor.
404 Such an approach would however still raise questions on how to explain any potential coupling to the
405 recently postulated syneresis or phase separation mechanism behind solidification, which is indeed
406 addressed by the present model. On the other hand, it is worth noting that if shear history is
407 considered the only mechanism behind fibre alignment, as in the present model, it is indeed hard to
408 justify why HME processing would yield any oriented fibres in the centre of the cooling die.

409 Additional mechanisms, e.g. extensional flow forming fibres in the core region of the die or pre-
410 oriented fibres from the barrel section may thus be of complementary value to the present model.
411 Future work may thus try to address any such discrepancies through further model development.

412

413 6. Conclusions

414 This study presents a simple model for predicting flow behaviour and fibre formation during high
415 moisture extrusion (HME) by incorporating the coupled effects of flow, temperature, phase
416 separation, fibre alignment and wall-slip. The results demonstrate that cooling temperature plays a
417 critical role in shaping the velocity profile, phase separation/syneresis and fibre alignment within the
418 extruder die. Specifically, the model indicates a balance between cooling temperature and plug flow
419 development to form oriented fibres near the die walls and randomly oriented fibres in the core
420 while maintaining feasible flow conditions.

421 The model's mean-field approach to wall-slip and phase separation offers a practical compromise
422 between physical accuracy and computational tractability. Validation through microscopy confirms
423 the model's ability to qualitatively reproduce the spatial distribution of fibre orientations observed in
424 the extrudate samples. However, model limitations remain, particularly in explaining any fibre
425 alignment in the die centre solely through shear history.

426 Future work should aim to refine the model by incorporating additional mechanisms, such as
427 extensional flow and barrel pre-orientation, and by quantifying fluid resistance to alignment through
428 e.g. dead stop experiments. These enhancements will likely improve the model's predictive capability
429 and support the development of more robust control strategies for fibre formation in HME
430 processing.

431

436

437 **Funding:** The Swedish Scientific Board Formas is gratefully acknowledged for funding of the present
438 study.

439

440 **Declaration of interest:** The authors at RISE Research Institutes of Sweden (RISE) have no individual
441 financial or personal gains from conducting and publishing the present original research.

442

443 7. References

444 Ardakani, H.A., Mitsoulis, E., & Hatzikiriakos, S.G. (2013). Polytetrafluoroethylene Paste Extrusion: A
445 Fibrillation Model and Its Relation to Mechanical Properties. *International Polymer Processing* 28(3),
446 306-313. <https://doi.org/10.3139/217.2744>.

447 Cahn, J.W., & Hilliard, J.E. (1958). Free Energy of a Nonuniform System. I. Interfacial Free Energy. *The
448 Journal of Chemical Physics* 28(2), 258-267. <https://doi.org/10.1063/1.1744102>.

449 Chen, F.L., Wei, Y.M., & Zhang, B. (2011). Chemical cross-linking and molecular aggregation of
450 soybean protein during extrusion cooking at low and high moisture content. *LWT - Food Science and
451 Technology* 44(4), 957-962. <https://doi.org/10.1016/j.lwt.2010.12.008>.

452 COMSOL, A. (2021). *COMSOL Multiphysics Reference Manual, version 6.0*", COMSOL, Inc,
453 www.comsol.com.

454 Cornet, S.H.V., Snel, S.J.E., Schreuders, F.K.G., van der Sman, R.G.M., Beyer, M., & van der Goot, A.J.
455 (2022). Thermo-mechanical processing of plant proteins using shear cell and high-moisture extrusion
456 cooking. *Critical Reviews in Food Science and Nutrition* 62(12), 3264-3280. <https://doi.org/10.1080/10408398.2020.1864618>.

457 Dekkers, B.L., Hamoen, R., Boom, R.M., & Van Der Goot, A.J. (2018). Understanding fiber formation in
458 a concentrated soy protein isolate - Pectin blend. *Journal of Food Engineering* 222, 84-92.
459 <https://doi.org/10.1016/j.jfoodeng.2017.11.014>.

460 Di, Y., Ding, L., Gao, L., & Huang, H. (2023). Association of meat consumption with the risk of
461 gastrointestinal cancers: a systematic review and meta-analysis. *BMC Cancer* 23(1), 782.
462 <https://doi.org/10.1186/s12885-023-11218-1>.

463 Folgar, F., & Tucker, C.L. (1984). Orientation Behavior of Fibers in Concentrated Suspensions. *Journal
464 of Reinforced Plastics and Composites* 3(2), 98-119. <https://doi.org/10.1177/073168448400300201>.

466 Gerber, P.J.S., H. Henderson, B. Mottet, A. , Opio, C., & Dijkman, J.F., A. Tempio, G., 2013. Tackling
 467 climate change through livestock – A global assessment of emissions and mitigation opportunities.
 468 Food and Agriculture Organization of the United Nations (FAO), Rome.

469 Glenn, A.J., Wang, F., Tessier, A.J., Manson, J.E., Rimm, E.B., Mukamal, K.J., Sun, Q., Willett, W.C.,
 470 Rexrode, K.M., Jenkins, D.J., & Hu, F.B. (2024). Dietary plant-to-animal protein ratio and risk of
 471 cardiovascular disease in 3 prospective cohorts. *American Journal of Clinical Nutrition* 120(6), 1373-
 472 1386. <https://doi.org/10.1016/j.ajcnut.2024.09.006>.

473 Grabowska, K.J., Tekidou, S., Boom, R.M., & van der Goot, A.-J. (2014). Shear structuring as a new
 474 method to make anisotropic structures from soy–gluten blends. *Food Research International* 64, 743-
 475 751. <https://doi.org/10.1016/j.foodres.2014.08.010>.

476 Guan, T., Sägesser, C., Villiger, R., Zychowski, L., Kohlbrecher, J., Dumpler, J., Mathys, A., Rühs, P.,
 477 Fischer, P., & Matsarskaia, O. (2024). In situ studies of plant-based meat analog texturization. *Food
 478 Hydrocolloids* 155, 110215. <https://doi.org/10.1016/j.foodhyd.2024.110215>.

479 Högg, E., Horneber, T., & Rauh, C. (2017). Experimental and numerical analyses of the texturisation
 480 process of a viscoelastic protein matrix in a cooling die after high moisture extrusion cooking.
 481 *Experimentelle Strömungsmechanik* 25.

482 Högg, E., Horneber, T., & Rauh, C. (2025). Modeling and experimental analysis of protein matrix
 483 solidification in cooling dies during high-moisture extrusion. *Frontiers in Food Science and Technology*
 484 Volume 5 - 2025. <https://doi.org/10.3389/frfst.2025.1443376>.

485 Kaunisto, E., Tsegaye, B., Kotzé, R., Wiklund, J., Kádár, R., & Stading, M. (2025). Towards in-line
 486 rheology measurement of protein melts during high moisture extrusion by pulsed ultrasound
 487 velocimetry. *Journal of Food Engineering* 391, in press. <https://doi.org/10.1016/j.jfoodeng.2024.112461>.

488 Kaunisto, E., Wassén, S., & Stading, M. (2024). A thermodynamical finite element model of the fibre
 489 formation process during extrusion of high-moisture meat analogues. *Journal of Food Engineering*
 490 362, 111760. <https://doi.org/10.1016/j.jfoodeng.2023.111760>.

491 Lorén, N., Altskär, A., Krona, A., Nilsson Pingel, T., Hall, S., Stading, M., & Öhgren, C. (2025).
 492 Combined Techniques to Understand the Multiscale Structure and Functionality of Foods. In G.
 493 Gillies, D. Rousseau (Eds.), *Soft Matter in Foods* (pp. 210-233). Royal Society of Chemistry,
 494 <https://doi.org/10.1039/9781837676699>.

495 Nieuwland, M., Heijnis, W., van der Goot, A.-J., & Hamoen, R. (2023). XRT for visualizing
 496 microstructure of extruded meat replacers. *Current Research in Food Science* 6, 100457.
 497 <https://doi.org/10.1016/j.crcfs.2023.100457>.

498 Osen, R., & Schweiggert-Weisz, U. (2016). High-moisture extrusion: Meat analogues.

499 Patil, P.D., Feng, J.J., & Hatzikiriakos, S.G. (2006). Constitutive modeling and flow simulation of
 500 polytetrafluoroethylene (PTFE) paste extrusion. *Journal of Non-Newtonian Fluid Mechanics* 139(1),
 501 44-53. <https://doi.org/10.1016/j.jnnfm.2006.05.013>.

502 Sandoval Murillo, J.L., Osen, R., Hiermaier, S., & Ganzenmüller, G. (2019). Towards understanding the
 503 mechanism of fibrous texture formation during high-moisture extrusion of meat substitutes. *Journal
 504 of Food Engineering* 242, 8-20. <https://doi.org/10.1016/j.jfoodeng.2018.08.009>.

505 Slattery, J.C. (1999). *Advanced Transport Phenomena*. Cambridge University Press, Cambridge.

506 Steinfeld, H., 2006. *Livestock's Long Shadow - Environmental Issues and Options*, FAO. Food and
 507 Agriculture Organization of the United Nations (FAO), Rome.

508 Sägesser, C., Mair, T., Braun, A., Dumpler, J., Fischer, P., & Mathys, A. (2025). Application of a shear
 509 cell for the simulation of extrusion to test the structurability of raw materials. *Food Hydrocoll.* 160,
 510 110736. <https://doi.org/10.1016/j.foodhyd.2024.110736>.

511 Tammi, R., Kaartinen, N.E., Harald, K., Maukonen, M., Tapanainen, H., Smith-Warner, S.A., Albanes,
 512 D., Eriksson, J.G., Jousilahti, P., Koskinen, S., Laaksonen, M.A., Heikkinen, S., Pitkäniemi, J., Pajari, A.-
 513 M., & Männistö, S. (2024). Partial substitution of red meat or processed meat with plant-based foods
 514 and the risk of colorectal cancer. *European Journal of Epidemiology* 39(4), 419-428. <https://doi.org/10.1007/s10654-024-01096-7>.

517 van der Sman, R.G.M., & van der Goot, A.J. (2023). Hypotheses concerning structuring of extruded
518 meat analogs. *Current Research in Food Science* 6, 100510. <https://doi.org/https://doi.org/10.1016/j.crefs.2023.100510>.

519

520 Vavlekas, D., Melo, L., Ansari, M., Grant, E., Fremy, F., McCoy, J.L., & Hatzikiriakos, S.G. (2017). Role
521 of PTFE paste fibrillation on Poisson's ratio. *Polymer Testing* 61, 65-73. <https://doi.org/https://doi.org/10.1016/j.polymertesting.2017.05.004>.

522

523 Wittek, P., Ellwanger, F., Karbstein, H.P., & Emin, M.A. (2021). Morphology Development and Flow
524 Characteristics during High Moisture Extrusion of a Plant-Based Meat Analogue. *Foods* 10(8), 1753.

525

526 Zhang, X., Zhao, Y., Zhang, T., Zhang, Y., Jiang, L., & Sui, X. (2022). High moisture extrusion of soy
527 protein and wheat gluten blend: An underlying mechanism for the formation of fibrous structures.
528 *LWT* 163, 113561. <https://doi.org/https://doi.org/10.1016/j.lwt.2022.113561>.

Figure 1. Comparison between the fitted explicit expression and implicit solutions for the equilibrium order parameter as a function of temperature.

Figure 2. Schematic picture of the simulated die geometry with the non-trivial boundary conditions.

Figure 3. Velocity magnitude, $|\mathbf{u}|$, and streamlines (black) in the cooling die at three different cooling temperatures for (A) $T_{cool} = 110 \text{ }^{\circ}\text{C}$, (B) $T_{cool} = 90 \text{ }^{\circ}\text{C}$ and (C) $T_{cool} = 60 \text{ }^{\circ}\text{C}$.

Figure 4. Outlet cross-sectional velocity profile, $|\mathbf{u}|$, for different cooling temperatures.

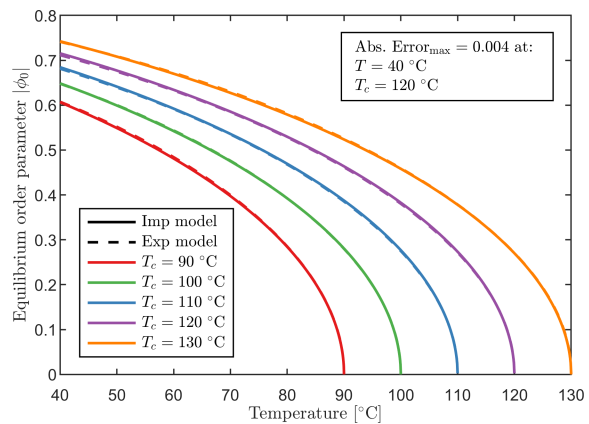
Figure 5. Local amount of phase separation, β , and streamlines (black) in the cooling die at three different cooling temperatures for (A) $T_{cool} = 100 \text{ }^{\circ}\text{C}$, (B) $T_{cool} = 90 \text{ }^{\circ}\text{C}$ and (C) $T_{cool} = 60 \text{ }^{\circ}\text{C}$.

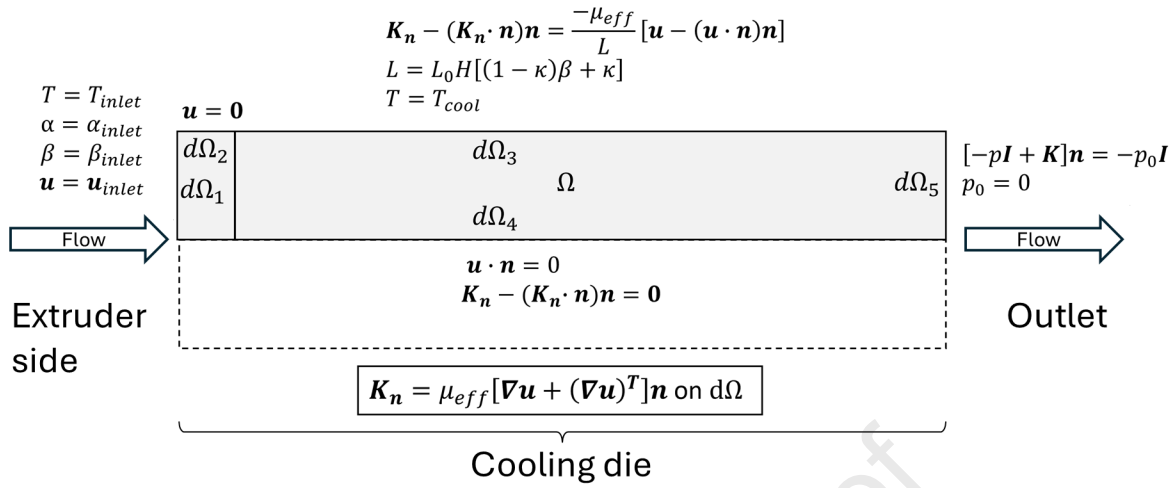
Figure 6. Fibre alignment measure, θ , in the cooling die and streamlines (black) for three different cooling temperatures for (A) $T_{cool} = 100 \text{ }^{\circ}\text{C}$, (B) $T_{cool} = 90 \text{ }^{\circ}\text{C}$ and (C) $T_{cool} = 60 \text{ }^{\circ}\text{C}$.

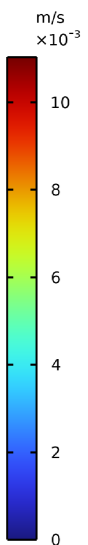
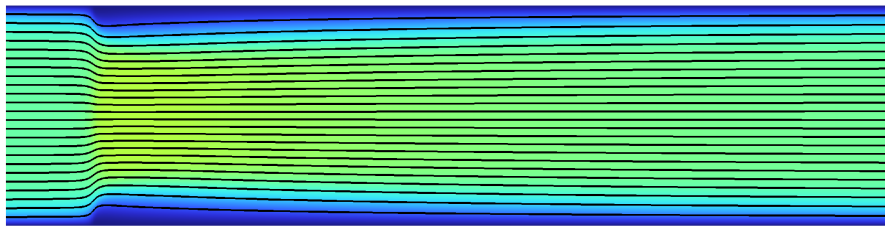
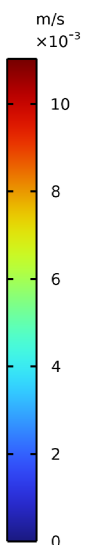
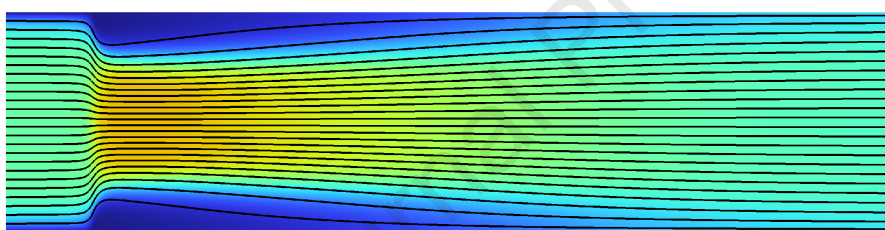
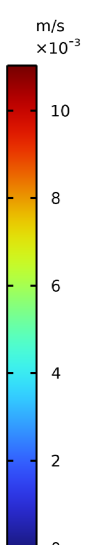
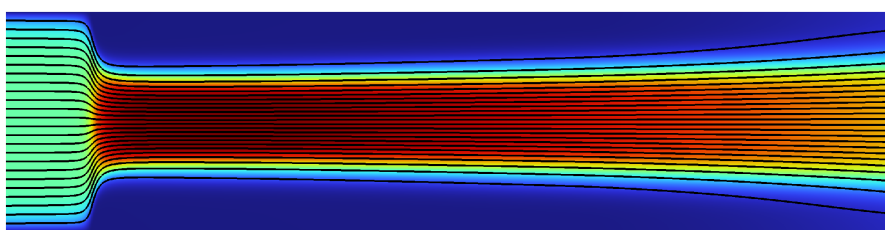
Figure 7. Composite fibre measures at $T_{cool} = 90 \text{ }^{\circ}\text{C}$ in the cooling die and streamlines (black) for (A) oriented fibres, F_o , and (B) randomly oriented fibres, F_{ro} .

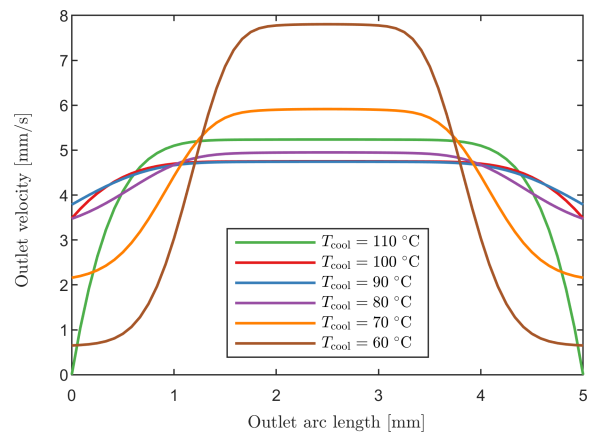
Figure 8. (A) LM image of the extrudate sample like in the simulations at lower magnification and at a position as indicated by the red frames, (B) CLSM image and (C-E) LM images of an extrudate at different magnifications and positions with (B-D) close to the edges and (E) in the centre. The

positions of (C) and (E) in (A) are indicated by the blue and black frames, respectively. The scale bars are (A) 200 μm , (B) 100 μm , (C) 50 μm and (D-E) 10 μm . Protein is shown in red in the CLSM image and in green in the LM images and fibres are green in the CLSM image and white in the LM image, where also starch is shown in violet.

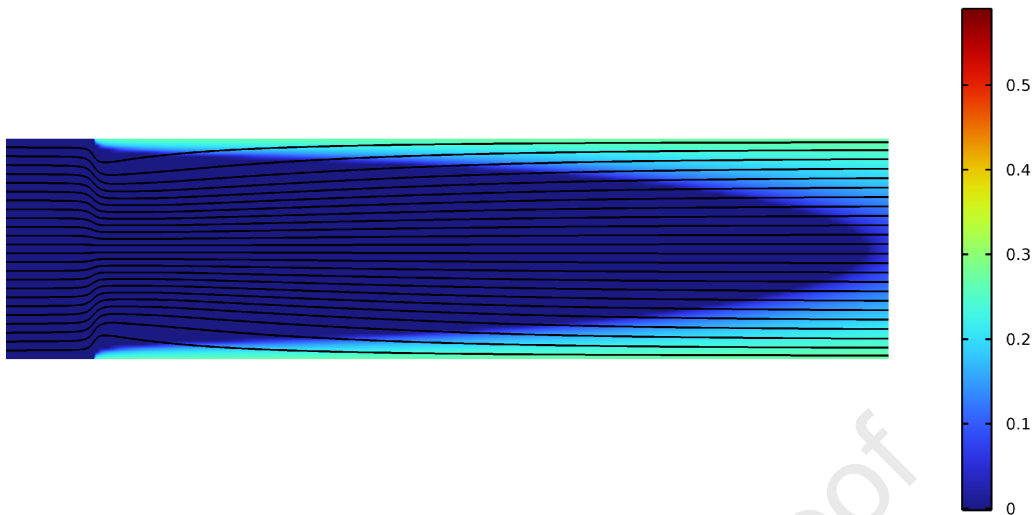
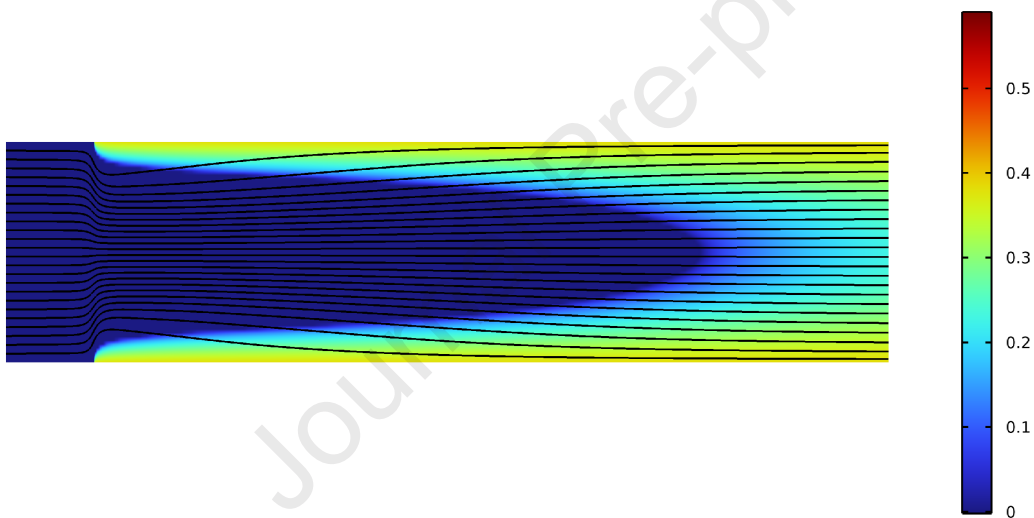
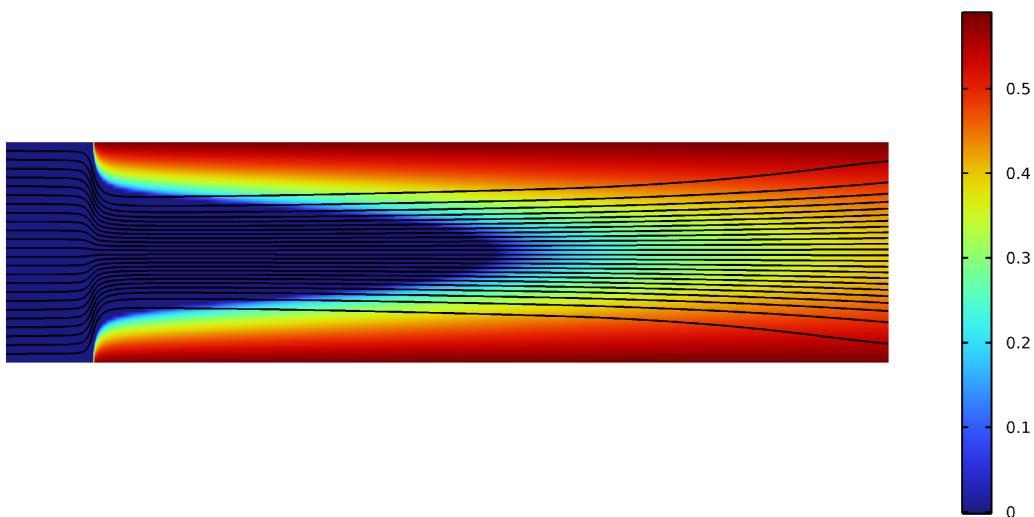


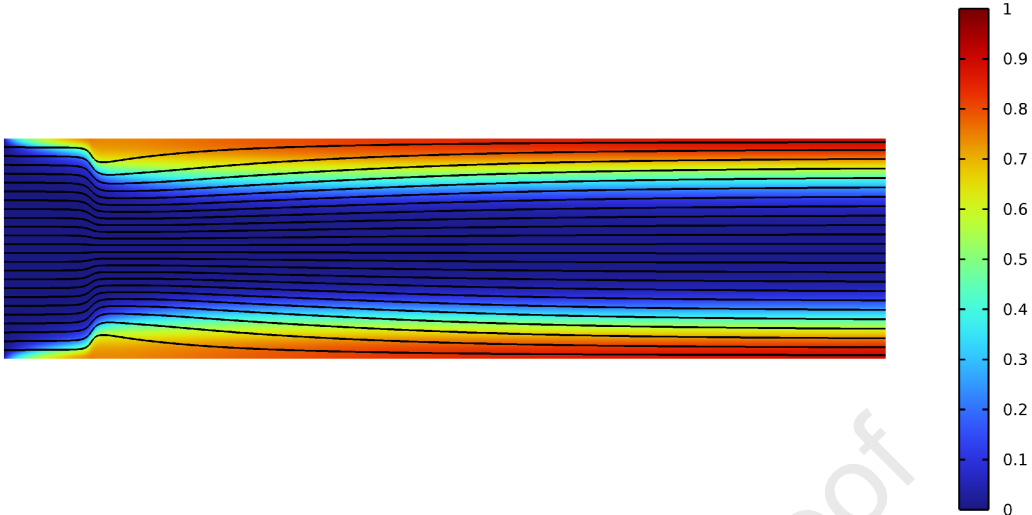
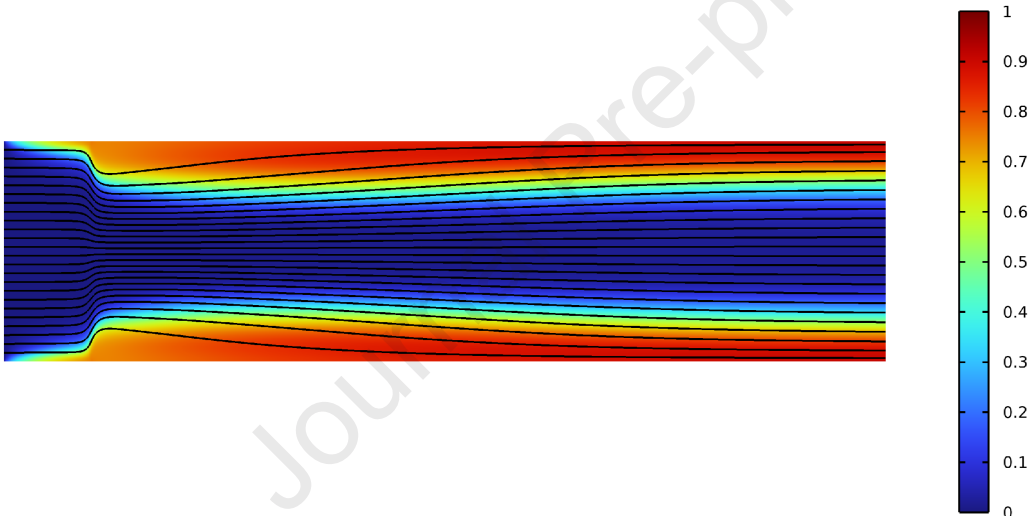
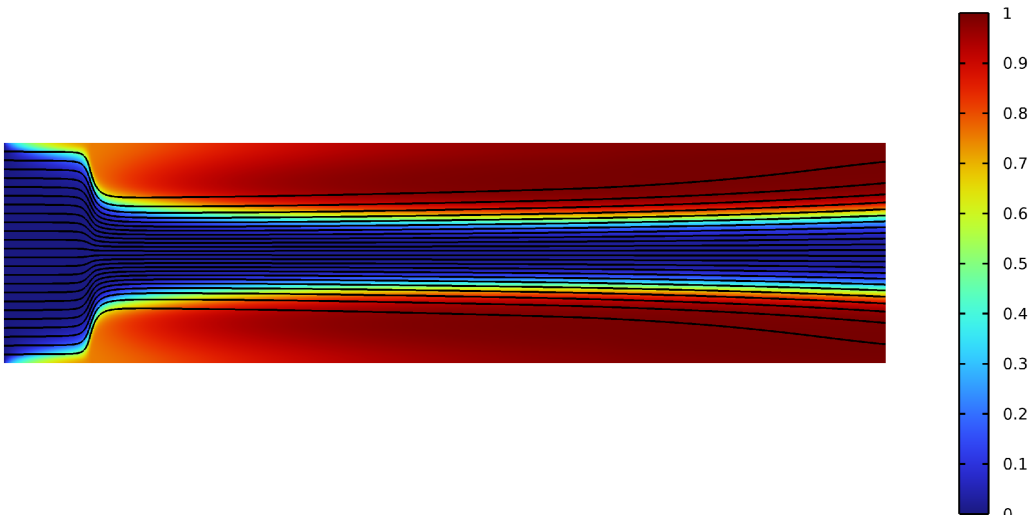


(A)**(B)****(C)**

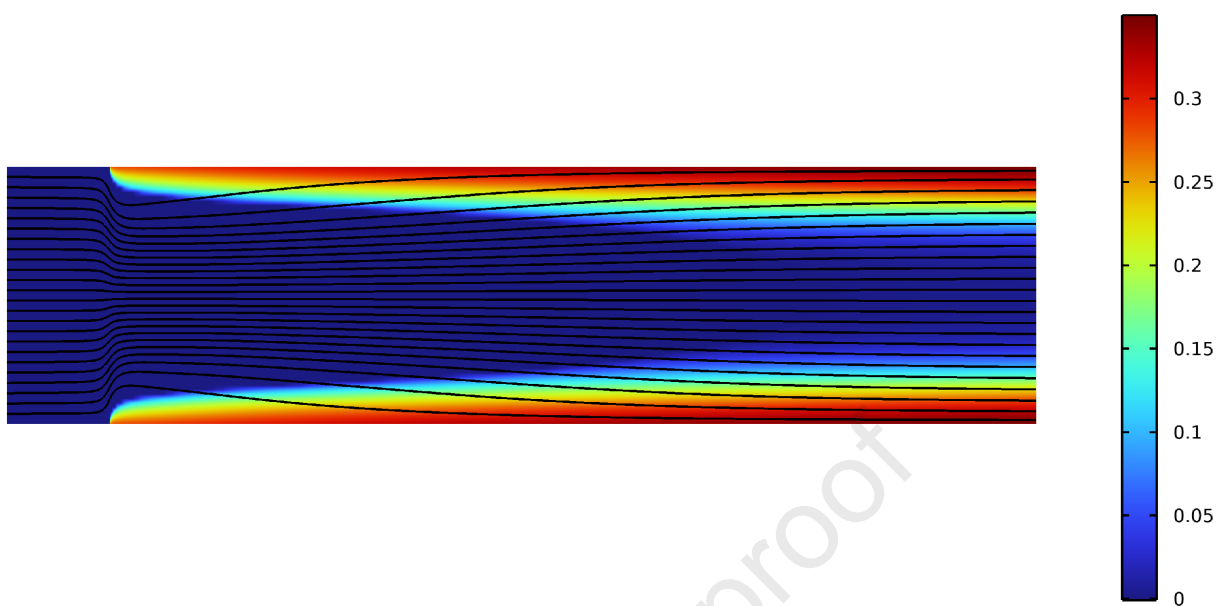


Journal Pre-proof

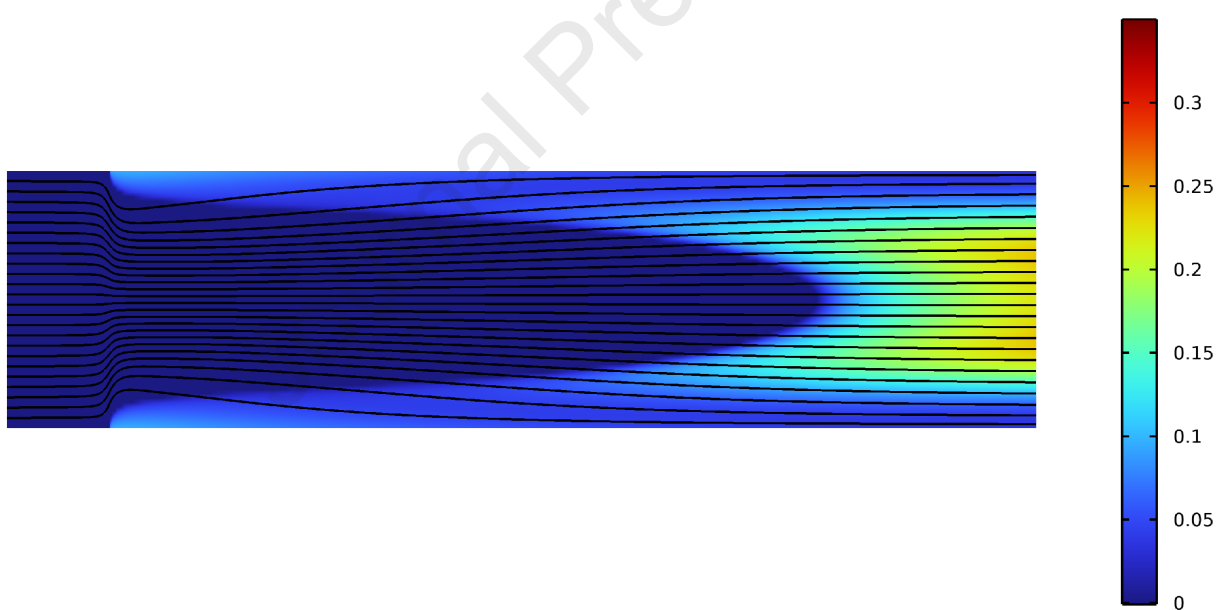
(A)**(B)****(C)**

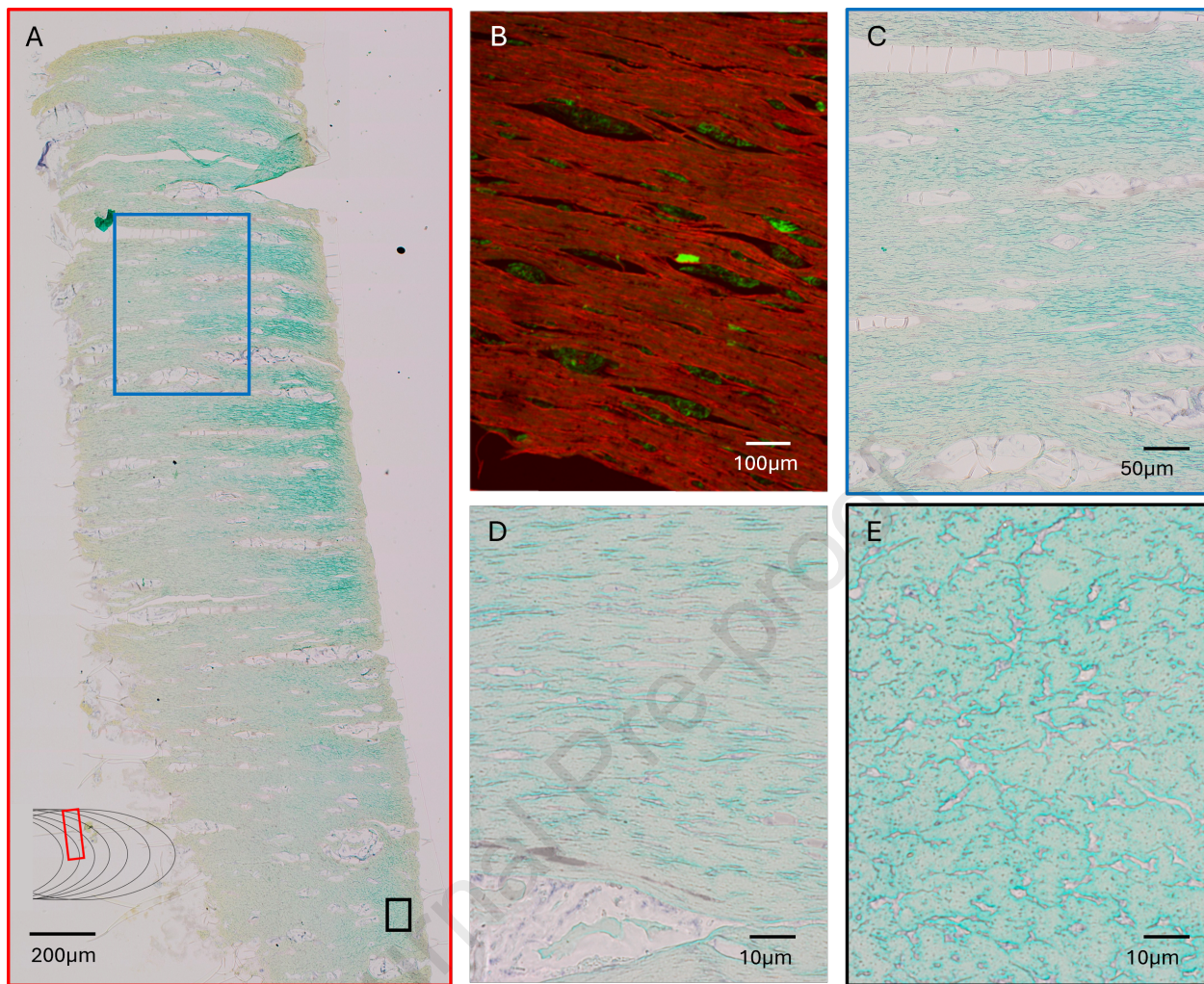
(A)**(B)****(C)**

(A)



(B)





Highlights:

- The model enables coupling relevant non-isothermal flow phenomena with fibre formation in the cooling die during high moisture extrusion.
- The impact of cooling temperature on plug flow transition is explained through a mean-field phase separation/syneresis dependent wall-slip condition.
- A simple shear history-dependent fibre alignment measure is proposed that enables a composite measure of fibre formation.
- Qualitative agreement between microscopy data and the location of predicted oriented and randomly oriented fibre domains in the extrudate is obtained.
- The model offers a practical coarse-grained alternative to solving the Cahn-Hilliard equation for prediction of fibre formation.

Declaration of interest statement

The authors at RISE Research Institutes of Sweden (RISE) have no individual financial or personal gains from conducting and publishing the present original research.